magnetochemistry

MDPI

Article

Process-Gas-Influenced Anti-Site Disorder and Its Effects on Magnetic and Electronic Properties of Half-Metallic Sr_2FeMoO_6 Thin Films

Ekta Yadav [1], Ketan S. Navale [1], Gulloo L. Prajapati [2] and Krushna R. Mavani [1,3,*]

[1] Department of Physics, Indian Institute of Technology (IIT) Indore, Khandwa Road, Simrol 453552, India; mscphd1807151002@iiti.ac.in (E.Y.); phd2101151022@iiti.ac.in (K.S.N.)
[2] Department of Physics, Indian Institute of Science Education and Research (IISER), Bhopal 462066, India; gulloo1992@gmail.com
[3] Centre for Advanced Electronics, Indian Institute of Technology (IIT), Indore 453552, India
* Correspondence: krushna@iiti.ac.in; Tel.: +91-731-6603318

Abstract: Anti-site disorder, arising due to the similar size of Fe and Mo ions in Sr_2FeMoO_6 (SFMO) double perovskites, hampers spintronic applicability by deteriorating the magnetic response of this double perovskite system. A higher degree of anti-site disorder can also completely destroy the half-metallicity of the SFMO system. To study the effects of different process gas conditions on the anti-site disorder, we have prepared a series of SFMO thin films on $SrTiO_3$ (001) single-crystal substrate using a pulsed laser deposition (PLD) technique. The films are grown either under vacuum or under N_2/O_2 partial gas pressures. The vacuum-grown SFMO film shows the maximum value of saturation magnetization (M_S) and Curie temperature (T_C), signaling the lowest anti-site disorder in this series. In other words, there is a long-range Fe/Mo-O-Mo/Fe ferrimagnetic exchange in the vacuum-grown thin film, thereby enhancing the magnetization. Further, all the SFMO films show a semiconducting state with a systematic increase in overall resistivity with the increased anti-site disorder. The electrical conduction mechanism is defined by the variable-range hopping model at low temperatures. Raman spectra show a weak Fano peak, suggesting the presence of electron–phonon coupling in SFMO thin films. These results show the significance of the process gas in causing anti-site disorder, tuning the degree of this disorder and therefore its influence on the structural, magnetic, electrical, and vibrational properties of SFMO thin films.

Keywords: double perovskites; half-metallic; thin films; anti-site disorder; spintronics; Fano; process gas

check for updates

Citation: Yadav, E.; Navale, K.S.; Prajapati, G.L.; Mavani, K.R. Process-Gas-Influenced Anti-Site Disorder and Its Effects on Magnetic and Electronic Properties of Half-Metallic Sr_2FeMoO_6 Thin Films. *Magnetochemistry* **2023**, *9*, 167. https://doi.org/10.3390/magnetochemistry9070167

Academic Editor: Devashibhai Adroja

Received: 26 May 2023
Revised: 18 June 2023
Accepted: 25 June 2023
Published: 28 June 2023

Copyright: © 2023 by the authors. Licensee MDPI, Basel, Switzerland. This article is an open access article distributed under the terms and conditions of the Creative Commons Attribution (CC BY) license (https://creativecommons.org/licenses/by/4.0/).

1. Introduction

Double perovskites with the chemical formula $A_2BB'O_6$ have has gained tremendous attention from the scientific community worldwide due to the flexibility of using various elemental compositions of A (i.e., rare earth or alkaline earth metal), B, and B′ ions (i.e., $3d/4d/5d$ elements), which drastically modify their properties [1,2]. These double perovskites exhibit fascinating fundamental properties and also have a wide range of applications in spin valves, data storage, tunnel junctions, etc., that can work at or above room temperature (RT) [3,4]. Among various double perovskites, Sr_2FeMoO_6 (SFMO) is one of the most promising conducting ferrimagnet double perovskites which has a high Curie temperature (T_C) ~415 K [3]. The discovery of low-field magnetoresistance (LFMR) at room temperature in sintered SFMO by Kobayashi et al. in 1998 opened up a new avenue for progressive research in spintronics [5,6]. SFMO consists of a half-metallic ground state with 100% spin polarization at the Fermi level [7,8]. The low-field magnetoresistance, high T_C and high spin-polarization make SFMO a promising potential candidate for spintronic devices, which can work well above RT as compared to low T_C-doped manganites [8].

SFMO exhibits an ordered double perovskite structure which crystallizes in the *I4/mmm* space group [9]. It consists of a regular arrangement of corner-sharing FeO_6 and MoO_6

octahedra which are three-dimensionally connected in an alternate pattern, and a Sr ion sits in the octahedral cavity. The ferrimagnetic coupling between alternately distributed Fe and Mo ions gives rise to a theoretically calculated saturation magnetization (M_S) of 4 μ_B/f.u. [10,11]. However, the experimentally observed value of M_S is smaller due to the presence of intrinsic anti-site defects [11]. These defects arise due to the possibility of the misoccupancy of Fe and Mo cations in the crystal due to a small difference in their ionic radii. The anti-site disorder destroys the long-range Fe-O-Mo arrangement in SFMO, thereby hampering the magnetic response and spintronic applicability of the system. Therefore, the fabrication of single-phase, chemically homogenous, epitaxial and B-site-ordered SFMO thin film is required in order to achieve the RT applications [10,12,13].

It is important to mention here that anti-site disorder and the physical properties of SFMO thin films are highly dependent on the synthesis conditions [10,14]. During the last few years, a lot of effort has been made to improve cation ordering in SFMO films. Amongst various thin-film deposition techniques, the pulsed laser deposition (PLD) method has been extensively used for synthesizing SFMO films at high deposition rates [11,15–18]. However, synthesizing high-quality stoichiometric SFMO thin films by PLD is still difficult due to various constraints in the deposition parameters [14]. A high substrate temperature is required to obtain sufficient atomic mobility for achieving a highly ordered double perovskite structure [16]. Moreover, very low oxygen partial pressure ($<10^{-4}$ mbar) is required, and a little oversupply of oxygen gives rise to undesirable phases such as $SrMoO_4$ and $SrFeO_3$ [10,11,14,18]. In some cases, vacuum and a reducing deposition environment (N_2 or H_2+Ar) can also be used to prepare phase-pure SFMO thin films [10,11,17]. However, achieving B-site ordering in SFMO films at ambient conditions is still under research.

In the present study, we have prepared a series of SFMO thin films in different deposition conditions on a $SrTiO_3$-STO (001) single-crystal substrate. The films are deposited either under vacuum, or under oxygen (O_2) and nitrogen (N_2) partial pressures. A substantial effect of background conditions (vacuum, N_2 and O_2) on cation-ordering is presented here, which eventually affects the structural, magnetic, vibrational, and electrical properties of SFMO thin films.

2. Experiment

A series of SFMO thin films was prepared on STO (001) single-crystal substrates using pulsed laser deposition (PLD) technique. Bulk polycrystalline pellet of SFMO was synthesized using standard solid-state reaction method. Stoichiometric amounts of high-purity (~99.99%) powders of $SrCO_3$, Fe_2O_3, and MoO_3 were ground and calcined at 900 °C for 12 h. The resulting mixture was reground and pressed into pellets using hydraulic press and then sintered at 1150 °C for 12 h in Ar +5% H_2 atmosphere. This pellet was used as target for thin film deposition in PLD. KrF excimer laser (λ = 248 nm, Coherent Compex Pro) with laser energy of 350 mJ and pulse repetition rate of 5 Hz was used for the depositions. The substrate temperature was 770 °C, and the target-to-substrate distance was 4 cm in the deposition chamber (Excel Instruments, Mumbai, India). The substrates were sequentially cleaned in acetone and propanol prior to the deposition. The films were grown under vacuum, under nitrogen (0.1 Pa, 0.5 Pa) and under oxygen (0.05 Pa) process gases. Just after deposition, the samples were cooled down to room temperature at 10 °C/minute.

To determine the phase purity and growth orientation, X-ray diffraction (XRD) measurements were performed using Bruker D2 Phaser Diffractometer (Karlsruhe, Germany) in Bragg–Brantano geometry with Cu k_α radiation. The magnetization measurements were performed using SQUID-VSM (Quantum Design, San Diego, CA, USA) magnetometer in the temperature range of 300 to 500 K and in a magnetic field ranging from −5T to 5T. The electrical properties were investigated by temperature-dependent resistivity measurements using a closed-cycle cryostat made by Janis Research, USA with a four-point probe method. Keithley (2612A), (Cleveland, OH, USA) source and measurements meters were used for the same. The vibrational properties were explored using Raman spectroscopy carried out using a Horiba LabRAM Raman microscope (Kyoto, Japan) equipped with charge coupled device

(CCD) detector. A *HeNe* laser with excitation light 633 nm was used with a laser power of 1 mW. All the micro-Raman scattered signals were collected in the back-scattering mode.

3. Results and Discussion

3.1. Structural Properties

To check the phase purity and growth orientation of the prepared SFMO films, XRD measurements were carried out as shown in Figure 1. It is clear from Figure 1a that the SFMO films grown under vacuum, 0.1 Pa N_2, 0.5 Pa N_2 and 0.05 Pa O_2 are in single phase and are highly oriented towards the *c*-axis. Since SFMO has a tetragonal crystal structure while STO is cubic, we considered the pseudocubic lattice parameter of SFMO for comparison. The pseudocubic lattice parameter of SFMO is 7.879 Å, corresponding to twice the lattice parameter equal to 7.81 Å for cubic STO. The lattice parameter of the STO substrate is less than that of the film material; therefore, the film experiences an in-plane compressive strain, which can be quantified as

$$strain\ (\%) = \frac{a_s - a_f}{a_s} \times 100 \quad (1)$$

where a_s and a_f are the lattice parameters of the substrate and film, respectively. Here, the lattice-mismatch-induced strain is -1.14%. While the material experiences an in-plane compression due to substrate-induced strain, an expansion of film material occurs towards the out-of-plane direction in order to accommodate the unit cell volume on the substrate. As a result, the film's XRD peak lies towards a lower 2θ value, which is evident from the enlarged view of (004) Bragg's reflection of the SFMO films shown in Figure 1b. It can be seen that the lattice parameter of the SFMO films grown does not vary much with the process gas and remains 8.09 ± 0.01 Å. On the Y-axis of the XRD plots, we show the intensity on a log-scale with an arbitrary unit. If we compare the ratio of the material's (004) peak intensity to the substrate's (002) peak intensity, for all the films, the ratio is very similar (0.26 ± 0.002). It can be observed from the plots that the FWHM of the vacuum-grown film is minimum This suggests the high crystallinity of the vacuum-grown film. With the increase in the background gas pressure, the FWHM of XRD peaks increases systematically, indicating decreased crystallinity. This could be attributed to the increased amount of anti-site disorder in SFMO films after the incorporation of a process gas, as suggested by previous reports [19].

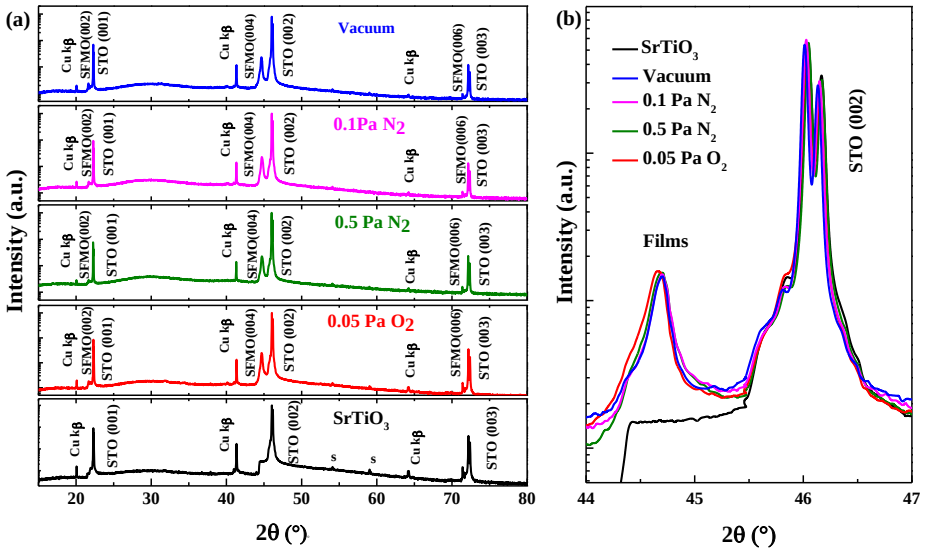

Figure 1. (**a**) XRD patterns of SFMO films deposited on STO (001) substrate using PLD under vacuum or under 0.1 Pa N_2, 0.5 Pa N_2, and 0.05 Pa O_2 partial pressure. The label "s" represents peaks from substrate having reflections other than (*00l*). (**b**) Magnified view of the (004) Bragg's reflection of the SFMO films deposited on STO (001) substrate.

3.2. Magnetic Properties

The effect of background conditions on the magnetic properties of SFMO thin films has been investigated using magnetic field and temperature-dependent magnetization measurements. Figure 2 shows the magnetic hysteresis (MH) loops collected at 300 K for the SFMO films grown under vacuum, with 0.1 Pa N_2 and 0.05 Pa O_2 pressures. The diamagnetic contribution from the STO substrate was eliminated from the data to present the actual magnetization of the SFMO films. The MH curves indicate the presence of macroscopic ferromagnetism in the SFMO thin films at room temperature. The SFMO film grown under vacuum shows the highest saturation magnetization (M_S), i.e., 2.5 μ_B/f.u., while the SFMO film grown under oxygen pressure shows the lowest M_S value, i.e., 1.25 μ_B/f.u. The M_S for nitrogen-grown SFMO film is 1.79 μ_B/f.u. It is clear from the data that the M_S of the SFMO films is lower than the theoretical predicted value, i.e., 4 μ_B/f.u. This could be attributed to several factors, such as oxygen vacancies, anti-site disorder, and non-stoichiometry in the Fe:Mo ratio which affects the magnetization [20]. Here, the SFMO film grown in oxygen has the lowest magnetization; the possibility of a reduction in magnetization due to oxygen vacancies can be ruled out. So, the decrement in saturation magnetization of the SFMO thin films could be attributed to the finite amount of anti-site disorder. Anti-site disorder reduces the net magnetization of the sample by destroying the specific spin arrangement of Fe and Mo sub-lattices without creating any significant effect on the individual magnetic moments at these sites.

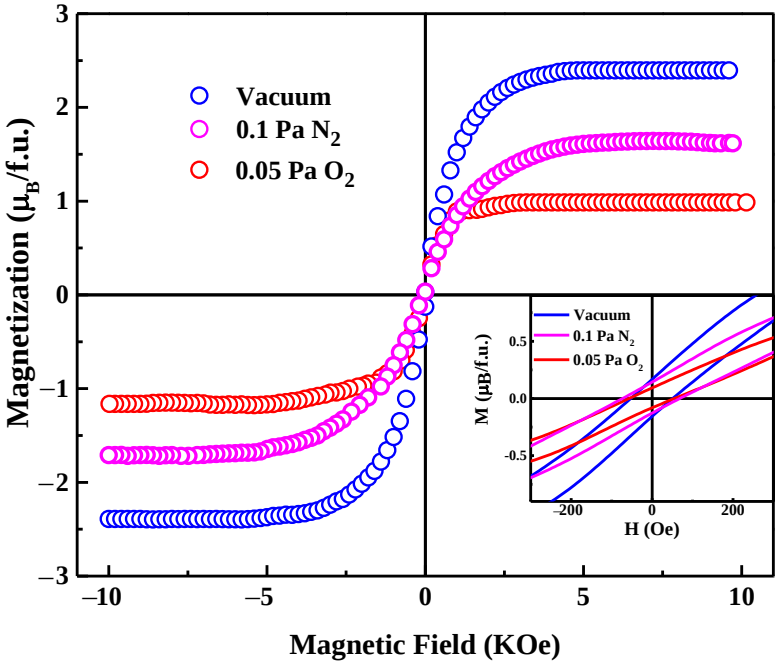

Figure 2. Magnetization versus magnetic field (MH) plots of SFMO films grown under vacuum, 0.1 Pa N_2, and 0.05 Pa O_2 partial pressure on STO (001). Inset shows the enlarged M versus H plots.

The strength of anti-site disorder present in these A_2FeMoO_6 compounds can be quantified as [20]:

$$M_S = (4 - 8\chi)\mu_B \quad (2)$$

where χ is the concentration of anti-site disorder and M_S is the saturation magnetization. The calculated value of anti-site disorder is 18.75%, and 27.6% and 34.3% for the SFMO films grown under vacuum, under 0.1 Pa N_2 and 0.05 Pa O_2 pressures, respectively. The present results suggest that vacuum-grown SFMO films exhibit the highest cation ordering, and the ordering decreases for nitrogen- and oxygen-grown films. The oxygen-grown SFMO film is highly disordered. The inset of Figure 2 shows the enlarged MH

hysteresis loops to display the coercive field. The coercive field for all the SFMO thin films is around 50–60 Oe. As the data density is low near zero field to see exact coercivity, we can say these are close by values.

The temperature-dependent magnetization (M vs. T) measurements were carried out for the SFMO films from 300 K to 550 K, as shown in Figure 3. The measurements were performed after field cooling the sample from 500 K down to 300 K with a magnetic field H = 100 Oe parallel to the film surface. It is clear from the figure that all the SFMO films display a ferromagnetic to paramagnetic (i.e., a Curie) transition, although the magnitude of the transition differs. The inset figures display the *dM/dT* plots, which show that the T_C of vacuum-, nitrogen-, and oxygen-grown SFMO films is about 420 K, 400 K, and 375 K, respectively. This decreased T_C value is also associated with increased anti-site disorder and antiferromagnetic regions that contribute to reducing the net magnetization. M versus T curves also suggest that the oxygen-grown SFMO film is highly disordered, and therefore it shows a very weak Curie transition of ~375 K.

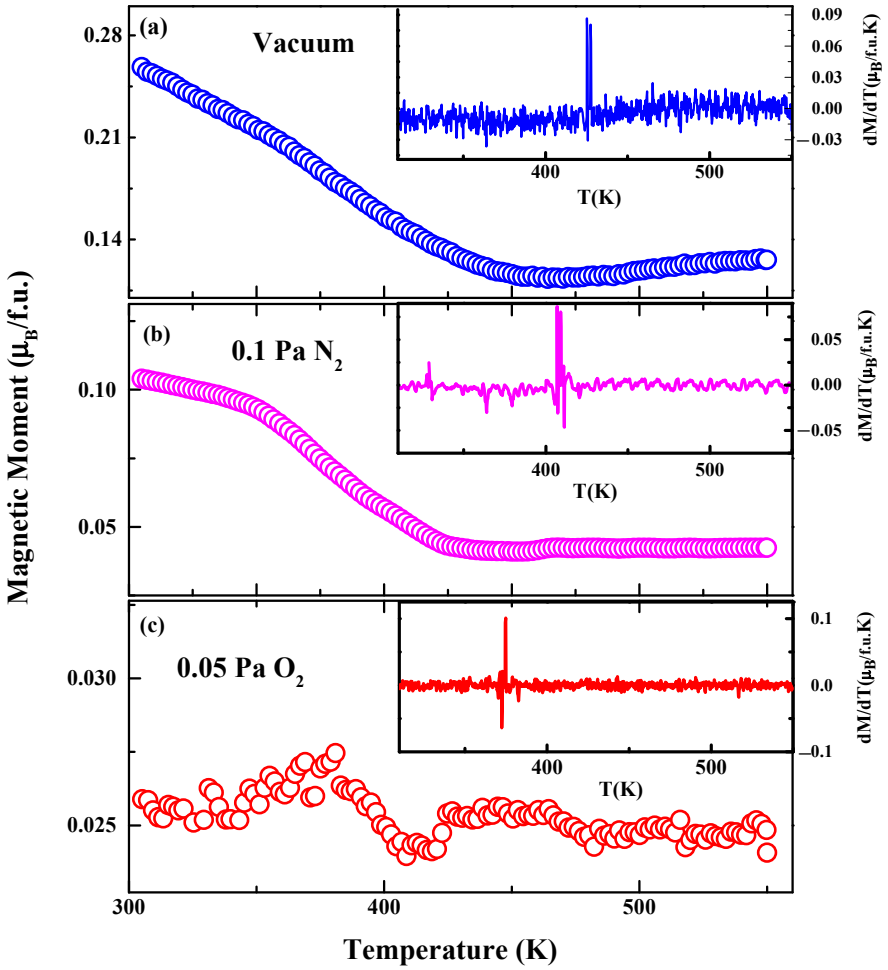

Figure 3. Magnetization versus temperature (MT) plots of SFMO thin films grown under vacuum, 0.1 Pa N_2, and 0.05 Pa O_2 partial pressure on STO (001). The inset figures show dM/dT versus T plots for SFMO films grown under vacuum, 0.1 Pa N_2, and 0.05 Pa O_2 partial pressures.

3.3. Surface Morphology

The surface morphology of the prepared series of thin films was investigated using atomic force microscopy (AFM) measurements. Figure 4a–c shows the 3D AFM images of SFMO films grown under vacuum, 0.1 Pa N_2, and 0.05 Pa O_2 pressures, respectively. It can be seen that all the films show similar surface morphology. The surface roughness of vacuum-, nitrogen- and oxygen-grown SFMO films is about 2 nm and the particle size is about 70 nm.

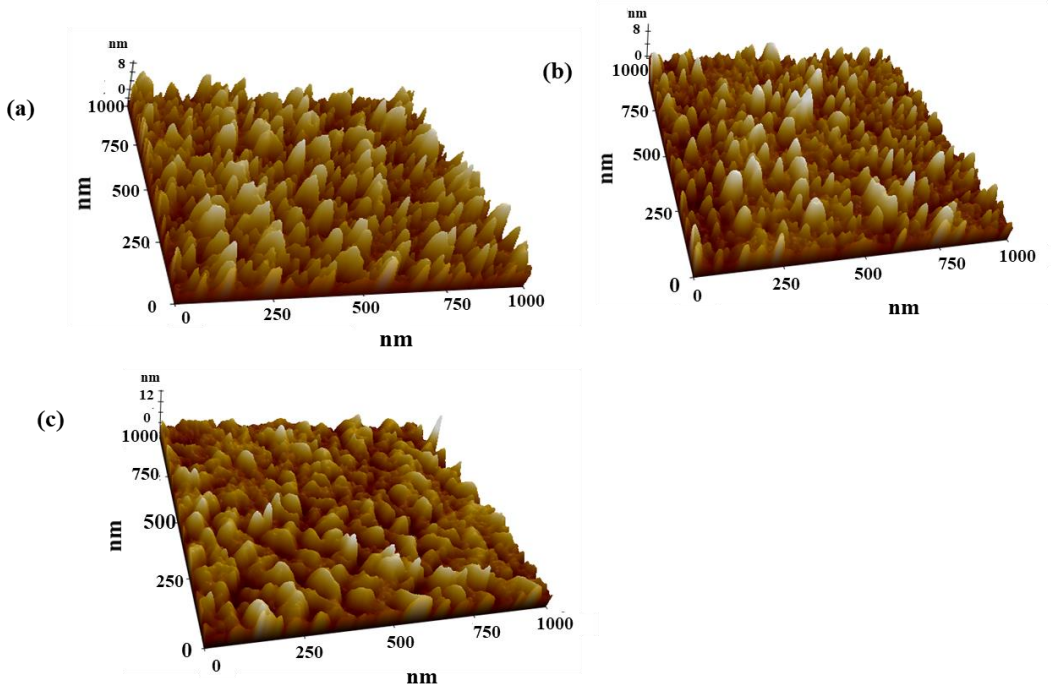

Figure 4. (**a**–**c**): AFM images of SFMO films grown under vacuum, 0.1 Pa N_2, and 0.05 Pa O_2 pressures.

3.4. Electrical Properties

It is reported that SFMO may exhibit a metallic, semiconducting, or insulating state depending on the synthesis methods, annealing temperature, and time, etc. [10,21]. To check the electrical properties, temperature-dependent resistivity measurements were carried out for all the SFMO films from 300 to 10 K. Figure 5 shows the resistivity vs. temperature plots for the SFMO films. All the SFMO films show semiconducting behavior ($d\rho/dT < 0$) with the room-temperature resistivity values in the order of several milliohm centimeters. Moreover, the SFMO film synthesized under vacuum exhibits lowest resistivity, and the overall resistivity of the films increases systematically with the increase in background gas pressure. The highest resistivity of oxygen-grown film is consistent with earlier observed results and is attributed to the increased anti-site defects [22].

In order to obtain a deeper insight in the semiconducting behavior, temperature-dependent resistivity data have been fitted with the variable-range hopping (VRH) model, in the temperature range 10–80 K, as described below [23]:

$$\rho(T) = \rho_0 \, exp\left(\frac{T_0}{T}\right)^{\frac{1}{4}} \tag{3}$$

where ρ_0 is the pre-exponential factor and T_0 stands for characteristic Mott temperature. This model applies at a lower temperature where conduction takes place only by the hopping of charge carriers. The value of the characteristic Mott temperature T_0 can be calculated by performing a linear fit on the $\ln(\rho)$ vs. $1/(T)^{1/4}$ plot. Furthermore, the characteristic Mott temperature can be defined as

$$T_0 = \frac{18}{k_B N(E_F)(\alpha)^3} \tag{4}$$

where $N(E_F)$ represents the density of states near the Fermi level and α is the localization length for the hopping of charge carriers. The temperature-dependent resistivity plots fitted with the VRH model are shown in Figure 6. The value of T_0 is shown in Table 1, which shows that T_0 increases with an increase in the background pressure. Earlier reports suggest that T_0 can be considered as an effective energy barrier between the localized

states and the extent of disorder in the disordered region [24]. A large value of T_0 implies higher disorder and/or large tilting of the BO_6 octahedra. Here, the SFMO film grown under vacuum has the lowest T_0, while the oxygen-grown SFMO film has the highest T_0 value. These results suggest the minimum disorder in vacuum-grown and the highest disorder in oxygen-grown SFMO films. These resistivity results corroborate well with the magnetization results.

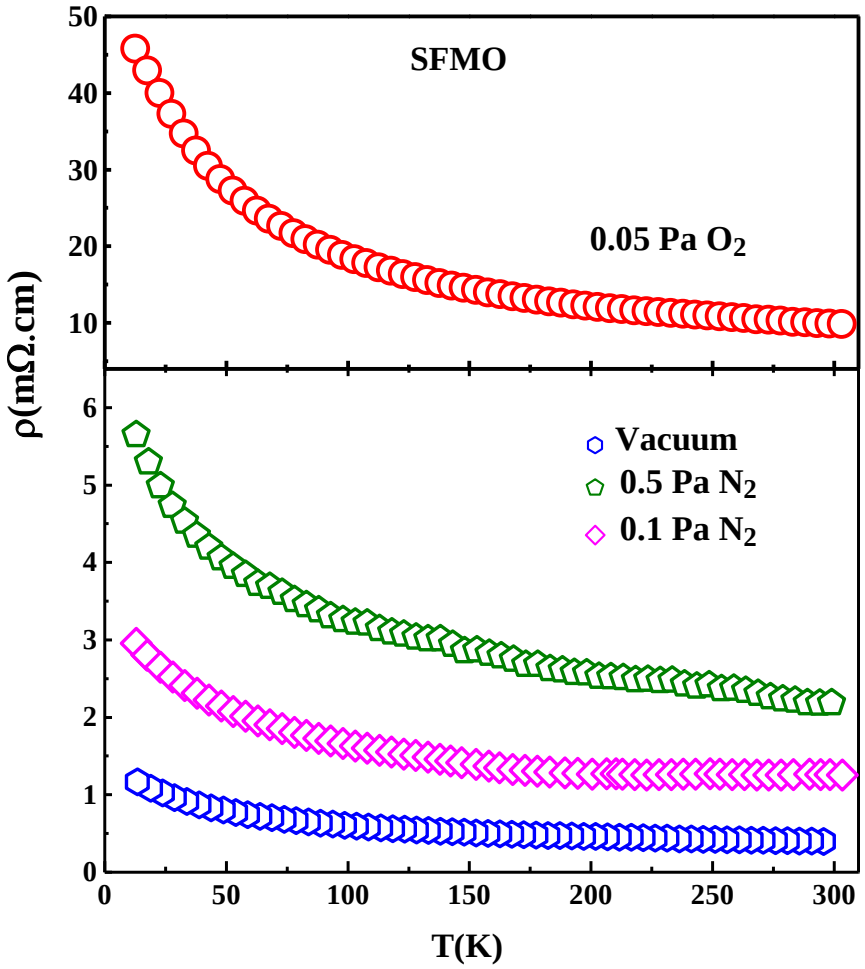

Figure 5. Temperature-dependent resistivity plots of SFMO films deposited under vacuum, 0.1 Pa N_2, 0.5 Pa N_2, and 0.05 Pa O_2 partial pressure.

Table 1. Mott temperature derived from the VRH fits on the temperature-dependent resistivity of Sr_2FeMoO_6 thin films.

Background Pressure (Pa)	Mott Temperature (10^4 K)
Vacuum (10^{-4})	2.20
0.1 N_2	2.75
0.5 N_2	3.45
0.05 O_2	3.77

3.5. Vibrational Properties

Micro-Raman spectroscopy gives insightful details about local structure, phase purity, and electron–phonon interactions in a material [25,26]. It can be noted that Raman spectroscopy of SFMO is less explored regardless of the extensive research carried out on this system. For the very first time, Son et al. carried out Raman spectroscopy on bulk SFMO in 2001 to show the phase decomposition of this double perovskite system [27]. In 2004, the

Raman spectra of highly aligned SFMO thin films grown on a $LaAlO_3$ single-crystal substrate were shown by Zhang et al. [28]. Raman spectroscopy of bulk SFMO was also carried out by Marrocchelli et al. in 2007 [29]. Both Zhang et al. and Marrocchelli et al. observed a phonon mode with asymmetric lineshape, known as the Fano feature, in the Raman spectra of SFMO. The Fano feature occurs due to a resonance between discrete phononic states with an electronic continuum, suggesting electron–phonon coupling in the system [28].

In the present case, Raman spectroscopy measurements were carried out on SFMO thin films grown on STO, as shown in Figure 7, with varying anti-site disorder. It is worth mentioning here that the STO substrate provides a huge background contribution; therefore, it is difficult to record Raman spectra of perovskite films grown on STO. As a result, only one B_g Raman mode around 455 cm^{-1} is observed in the Raman spectra of SFMO films, as shown in Figure 7. This B_g Raman mode results from the vibrations of strontium–oxygen bonds of SFMO [28]. The asymmetric lineshape of the B_g Raman mode (Fano feature) indicates a strong coupling between the phononic and electronic states in SFMO films. From Figure 7, it is clear that the Fano peak is highly asymmetric, well-defined, and sharp in the Raman spectrum of vacuum-grown SFMO film, implying stronger electron–phonon coupling in the film. With an increase in the anti-site disorder, the asymmetry of the Fano peak decreases systematically for the SFMO films grown in different process gases, which indicates that electron–phonon interaction decreases. This gradual change with anti-site disorder is also indirectly observed by magnetization measurements, as also mentioned earlier. The Fano feature is very weak in the oxygen-grown SFMO film which has a high anti-site disorder and less electron–phonon coupling. Thus, a sharp Fano feature of SFMO materials indicates a reduced anti-site disorder in this system.

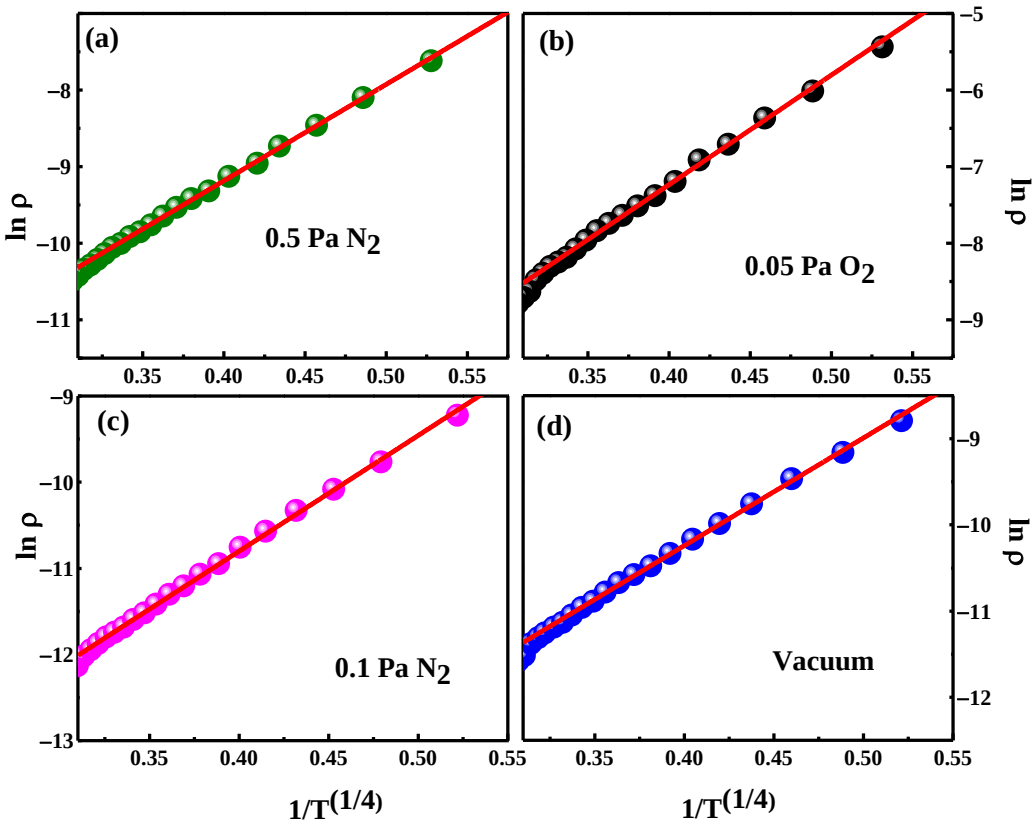

Figure 6. (**a**–**d**): Variable-range hopping (VRH) model fitting to the resistivity plots of SFMO films. The symbols represent the experimental data and the red line shows the fits.

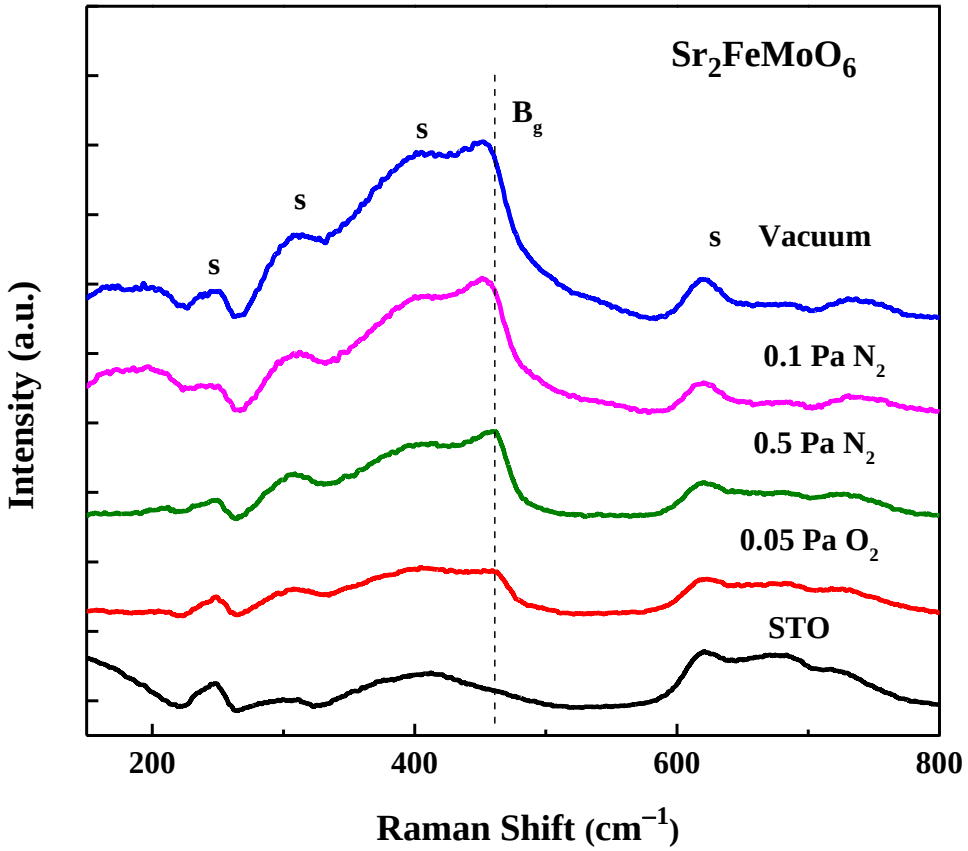

Figure 7. Raman spectra of SFMO films deposited on STO under vacuum, 0.1 Pa N_2, 0.5 Pa N_2, and 0.05 Pa O_2 partial pressures. The label "s" denotes the Raman modes originating from STO substrate.

4. Conclusions

A series of SFMO thin films were deposited on an STO (001) single-crystal substrate in different process gasses or under vacuum. The phase purity and crystallinity of SFMO films is affected by these different background conditions. The vacuum-grown SFMO film displays good crystallinity and the highest value of saturation magnetization and Curie temperature amongst these films. These features confirm a higher degree of B-site cation ordering and long-range Fe-O-Mo ferrimagnetic interactions in vacuum-grown SFMO. On the other hand, the reduced M_S and T_C values for other SFMO films grown under oxygen and nitrogen gases indicate increased anti-site defects, which destroy the ferromagnetic interactions in the system. A systematic variation in M_S with increased anti-site disorder in these films clearly indicates that the process gas has a defining role in changing this disorder in SFMO double perovskites. Further, the overall resistivity of the SFMO films increases systematically with the degree of anti-site disorder. The parameters obtained using the VRH model also indicate an increased disorder in the films grown under background gas pressure, as compared to that grown under vacuum. A Fano feature is observed in the Raman spectra, indicating the presence of electron–phonon interactions in SFMO films. A stronger Fano feature appears for the vacuum-grown film, clearly suggesting stronger electron–phonon interactions because of reduced anti-site disorder. These results present the gradually changing anti-site disorder in SFMO films and its systematically varied effects on the physical properties of SFMO thin films.

Author Contributions: E.Y.: Methodology, Investigation, Data curation, Formal analysis, Writing—original draft, Writing—review and editing; K.S.N.: Writing—review and editing; G.L.P.: Data curation; K.R.M.: Conceptualization, Validation, Supervision, Funding acquisition, Writing—review and editing. All authors have read and agreed to the published version of the manuscript.

Funding: E.Y. acknowledges CSIR, New Delhi, for providing fellowship through grant no. 1061751693. K.S.N. acknowledges DST for providing fellowship through INSPIRE grant no. IF200306. The facility of Raman Spectrometer under DST-FIST project no. SR/FST/PSI-225/2016 of Discipline of Physics, IIT Indore, is also acknowledged.

Institutional Review Board Statement: Not applicable.

Informed Consent Statement: Not applicable.

Data Availability Statement: Data can be made available from corresponding author on request.

Acknowledgments: SIC, IIT Indore is acknowledged for extending AFM facility.

Conflicts of Interest: The authors declare no conflict of interest.

References

1. Prellier, W.; Smolyaninova, V.; Biswas, A.; Galley, C.; Greene, R.L.; Ramesha, K.; Gopalakrishnan, J. Properties of the ferrimagnetic double perovskites A_2FeReO_6 (A = Ba and Ca). *J. Phys. Condens. Matter* **2000**, *12*, 965–973. [CrossRef]
2. Anderson, M.T.; Greenwood, K.B.; Taylor, G.A.; Poeppelmeier, K.R. B-cation arrangements in double perovskites. *Prog. Solid State Chem.* **1993**, *22*, 197–233. [CrossRef]
3. Saxena, M.; Tanwar, K.; Maiti, T. Environmental friendly Sr_2TiMoO_6 double perovskite for high temperature thermoelectric applications. *Scr. Mater.* **2017**, *130*, 205–209. [CrossRef]
4. Azuma, M.; Takata, K.; Saito, T.; Ishiwata, S.; Shimakawa, Y.; Takano, M. Designed ferromagnetic, ferroelectric Bi_2NiMnO_6. *J. Am. Chem. Soc.* **2005**, *127*, 8889–8892. [CrossRef]
5. Kobayashi, K.-I.; Kimura, T.; Sawada, H.; Terakura, K.; Tokura, Y. Room-temperature magnetoresistance in an oxide material with an ordered double-perovskite structure. *Nature* **1998**, *395*, 677–680. [CrossRef]
6. Serrate, D.; Teresa, J.M.D.; Ibarra, M.R. Double perovskites with ferromagnetism above room temperature. *J. Phys. Condens. Matter* **2006**, *19*, 023201. [CrossRef]
7. Kim, T.H.; Uehara, M.; Cheong, S.-W.; Lee, S. Large room-temperature intergrain magnetoresistance in double perovskite $SrFe_{1-x}(MoorRe)_xO_3$. *Appl. Phys. Lett.* **1999**, *74*, 1737–1739. [CrossRef]
8. Tomioka, Y.; Okuda, T.; Okimoto, Y.; Kumai, R.; Kobayashi, K.-I.; Tokura, Y. Magnetic and electronic properties of a single crystal of ordered double perovskite Sr_2FeMoO_6. *Phys. Rev. B* **2000**, *61*, 422–427. [CrossRef]
9. Cernea, M.; Vasiliu, F.; Plapcianu, C.; Bartha, C.; Mercioniu, I.; Pasuk, I.; Lowndes, R.; Trusca, R.; Aldica, G.V.; Pintilie, L. Preparation by sol–gel and solid state reaction methods and properties investigation of double perovskite Sr_2FeMoO_6. *J. Eur. Ceram. Soc.* **2013**, *33*, 2483–2490. [CrossRef]
10. Shinde, S.R.; Ogale, S.B.; Greene, R.L.; Venkatesan, T.; Tsoi, K.; Cheong, S.-W.; Millis, A.J. Thin films of double perovskite Sr_2FeMoO_6: Growth, optimization, and study of the physical and magnetotransport properties of films grown on single-crystalline and polycrystalline SrTiO3 substrates. *J. Appl. Phys.* **2003**, *93*, 1605–1612. [CrossRef]
11. Santosh, M.; Lacotte, M.; David, A.; Boullay, P.; Grygiel, C.; Pravarthana, D.; Rohrer, G.S.; Salvador, P.A.; Padhan, P.; Lüders, U.; et al. Pulsed laser deposition of Sr_2FeMoO_6 thin films grown on spark plasma sintered Sr_2MgWO_6 substrates. *J. Phys. Appl. Phys.* **2017**, *50*, 235301. [CrossRef]
12. Jalili, H.; Heinig, N.F.; Leung, K.T. X-ray photoemission study of Sr_2FeMoO_6 and $SrMoO_4$ films epitaxially grown on MgO(001): Near-surface chemical-state composition analysis. *Phys. Rev. B* **2009**, *79*, 174427. [CrossRef]
13. Du, C.; Adur, R.; Wang, H.; Hauser, A.J.; Yang, F.; Hammel, P.C. Control of Magnetocrystalline Anisotropy by Epitaxial Strain in Double Perovskite Sr_2FeMoO_6 Films. *Phys. Rev. Lett.* **2013**, *110*, 147204. [CrossRef]
14. Suchaneck, G.; Kalanda, N.; Artsiukh, E.; Gerlach, G. Challenges in $Sr_2FeMoO_6-\delta$ Thin Film Deposition. *Phys. Status Solidi B* **2020**, *257*, 1900312. [CrossRef]
15. Song, J.H.; Park, B.-G.; Park, J.-H.; Jeong, Y.H. Double-Perovskite Sr_2FeMoO_6 Thin Films Prepared by Using Pulsed Laser Deposition: Growth and Crystal, Electronic and Magnetic Structures. *J. Korean Phys. Soc.* **2008**, *53*, 1084–1088. [CrossRef]
16. Kumar, D.; Kaur, D. Substrate-dependent structural and magnetic properties of Sr_2FeMoO_6 nanostructured double perovskite thin films. *Phys. B Condens. Matter Phys. B* **2010**, *405*, 3259–3266. [CrossRef]
17. Sanchez, D.; Auth, N.; Jakob, G.; Martínez, J.L.; García-Hernández, M. Pulsed laser deposition of Sr_2FeMoO_6 thin films. *J. Magn. Magn. Mater.* **2005**, *294*, e119–e122. [CrossRef]
18. Borges, R.P.; Lhostis, S.; Bari, M.A.; Versluijs, J.J.; Lunney, J.G.; Coey, J.M.D.; Besse, M.; Contour, J.-P. Thin films of the double perovskite Sr_2FeMoO_6 deposited by pulsed laser deposition. *Thin Solid Films* **2003**, *429*, 5–12. [CrossRef]
19. Kim, K.-W.; Ghosh, S.; Buvaev, S.; Mhin, S.; Jones, J.L.; Hebard, A.F.; Nortan, D.P. The effects of oxygen pressure on disordering and magneto-transport properties of Ba_2FeMoO_6 thin films grown via pulsed laser deposition. *J. Appl. Phys.* **2015**, *118*, 033903. [CrossRef]
20. Qian, Y.; Wu, H.; Lu, R.; Tan, W.; Xiao, C.; Deng, K. Effect of High-Pressure on the Electronic and Magnetic Properties in Double Perovskite Oxide Sr_2FeMoO_6. *J. Appl. Phys.* **2012**, *112*, 103712. [CrossRef]
21. Zhang, J.S.; Yu, R.C.; Li, F.Y.; Li, X.D.; Liu, J.; Feng, C.G.; Jin, C.Q. Strucutral stability and electrical properties of $Sr_2Fe_{1+x}Mo_{1-y}O_{6-\delta}$ under high pressure. *J. Ally. Compds.* **2004**, *3482*, 67.

22. Sánchez, D.; García-Hernández, M.; Auth, N.; Jakob, G. Structural, magnetic, and transport properties of high-quality epitaxial Sr_2FeMoO_6 thin films prepared by pulsed laser deposition. *J. Appl. Phys.* **2004**, *96*, 2736–2742. [CrossRef]
23. Paul, D.K.; Mitra, S.S. Evaluation of Mott's parameters for hopping conduction in amorphous Ge, Si, and Se-Si. *Phys. Rev. Lett.* **1973**, *31*, 1000–1003. [CrossRef]
24. Zhai, Y.; Qiao, J.; Huo, G.; Han, S. Synthesis, magnetic and electrical transport properties of magnetoresistance material Sr2FeMoO6 by microwave sintering. *J. Magn. Magn. Mater.* **2012**, *324*, 2006–2010. [CrossRef]
25. Weber, M.C.; Kreisel, J.; Thomas, P.A.; Newton, M.; Sardar, K.; Walton, R.I. Phonon Raman scattering of $RCrO_3$ perovskites (R = Y, La, Pr, Sm, Gd, Dy, Ho, Yb, Lu). *Phys. Rev. B* **2012**, *85*, 054303. [CrossRef]
26. Yadav, E.; Harisankar, S.; Soni, K.; Mavani, K.R. Effects of Cu-doping on the vibrational and electronic properties of epitaxial $PrNiO_3$ thin films. *Vib. Spectrosc.* **2021**, *112*, 103185. [CrossRef]
27. Son, L.H.; Phuc, N.X.; Phuc, P.V.; Hong, N.M.; Hong, L.V. Observation of phase decomposition of Sr_2FeMoO_6 by Raman spectroscopy. *J. Raman Spectrosc.* **2001**, *32*, 817–820. [CrossRef]
28. Zhang, T.; Branford, W.R.; Trodahl, H.J.; Sharma, A.; Rager, J.; MacManus-Driscoll, J.L.; Cohen, L.F. Raman spectroscopy of highly aligned thin films of Sr_2FeMoO_6. *J. Raman Spectrosc.* **2004**, *35*, 1081–1085. [CrossRef]
29. Marrocchelli, D.; Postorino, P.; Di Castro, D.; Arcangeletti, E.; Dore, P.; Cestelli Guidi, M.; Ray, S.; Sarma, D.D. Pressure and temperature dependence of the Fano resonance in the Raman spectrum of A_2FeMoO_6 systems (A = Sr, Ca). *Phys. Rev. B Condens. Matter Mater. Phys.* **2007**, *76*, 172405. [CrossRef]

Disclaimer/Publisher's Note: The statements, opinions and data contained in all publications are solely those of the individual author(s) and contributor(s) and not of MDPI and/or the editor(s). MDPI and/or the editor(s) disclaim responsibility for any injury to people or property resulting from any ideas, methods, instructions or products referred to in the content.